

Cite this: *RSC Adv.*, 2018, 8, 41491

# Supported binary CuO<sub>x</sub>–Pt catalysts with high activity and thermal stability for the combustion of NH<sub>3</sub> as a carbon-free energy source†

Saaya Kiritoshi,<sup>a</sup> Takeshi Iwasa,<sup>b</sup> Kento Araki,<sup>a</sup> Yusuke Kawabata,<sup>a</sup> Tetsuya Taketsugu,<sup>b</sup> Satoshi Hinokuma<sup>b\*</sup> and Masato Machida<sup>a</sup>

Recently, NH<sub>3</sub> has been thought to be a renewable and carbon-free energy source. The use of NH<sub>3</sub> fuel, however, is hindered by its high ignition temperature and N<sub>2</sub>O/NO production. To overcome these issues, in this study, the combustion of NH<sub>3</sub> over copper oxide (CuO<sub>x</sub>) and platinum (Pt) catalysts supported on aluminium silicates (3Al<sub>2</sub>O<sub>3</sub>·2SiO<sub>2</sub>), aluminium oxides (Al<sub>2</sub>O<sub>3</sub>), and silicon oxides (SiO<sub>2</sub>) were compared. To achieve high catalytic activity for the combustion of NH<sub>3</sub> and high selectivity for N<sub>2</sub> (or low selectivity for N<sub>2</sub>O/NO), conditions for the preparation of impregnated binary catalysts were optimised. With respect to the binary catalysts, sequentially impregnated CuO<sub>x</sub>/Pt/Al<sub>2</sub>O<sub>3</sub> exhibited relatively higher activity, N<sub>2</sub> selectivity, and thermal stability. From XRD and XAFS analyses, CuO<sub>x</sub> and Pt in CuO<sub>x</sub>/Pt/Al<sub>2</sub>O<sub>3</sub> were present as CuAl<sub>2</sub>O<sub>4</sub> and metallic Pt, respectively. Given that the combustion activity was closely associated with the Pt nanoparticle size, which was estimated from the Scherrer equation and the pulsed CO technique, highly dispersed Pt nanoparticles were crucial for the low-temperature light-off of NH<sub>3</sub>. For single and binary catalysts, although NH (imide) deformation modes as a key species for N<sub>2</sub>O production were detected by *in situ* FTIR spectral analysis, the band intensity of CuO<sub>x</sub>/Pt/Al<sub>2</sub>O<sub>3</sub> was less than those of CuO<sub>x</sub>/Al<sub>2</sub>O<sub>3</sub> and Pt/Al<sub>2</sub>O<sub>3</sub>. Therefore, CuO<sub>x</sub>/Pt/Al<sub>2</sub>O<sub>3</sub> exhibits high selectivity for N<sub>2</sub> in NH<sub>3</sub> combustion.

Received 25th September 2018  
Accepted 27th November 2018

DOI: 10.1039/c8ra07969b

rsc.li/rsc-advances

## Introduction

Recent studies have reportedly considered NH<sub>3</sub> to serve not only as a H<sub>2</sub> carrier material but also as a renewable, carbon-free energy source because of its high energy density (3160 W h L<sup>-1</sup>) and negligible thermal NO<sub>x</sub> emission.<sup>1</sup> Currently, NH<sub>3</sub> is industrially produced at a high pressure using N<sub>2</sub> (produced from air) and H<sub>2</sub> (produced from natural gas) by employing the Haber–Bosch process, which consumes a large amount of energy. However, the energy and costs associated with H<sub>2</sub> production and natural gas is 70–90% of that required for NH<sub>3</sub> production.<sup>2</sup> Therefore, the low energy and costs that are associated with H<sub>2</sub>

production along with the fact that it is a renewable energy source should be emphasised to ensure that the society utilises H<sub>2</sub> along with NH<sub>3</sub>. As a proof-of-concept for using NH<sub>3</sub> as a fuel, an NH<sub>3</sub>-fuelled micro-gas turbine has been employed to demonstrate the potential of NH<sub>3</sub>-fired power plants at the Fukushima Renewable Energy Institute in Japan, as well as an NH<sub>3</sub>-fuelled industrial furnace.<sup>3</sup> Compared to fossil fuels, however, NH<sub>3</sub> exhibits disadvantages of a high ignition temperature, low combustion rate, and N<sub>2</sub>O/NO<sub>x</sub> production. Therefore, to overcome these issues, it is imperative to develop a novel NH<sub>3</sub> combustion system. First, a catalytic NH<sub>3</sub> combustion system, which decreases the ignition temperature and N<sub>2</sub>O/NO<sub>x</sub> emissions, was developed. Previously, our group has successfully developed a catalytic NH<sub>3</sub> combustion system and novel catalysts exhibiting high activity, N<sub>2</sub> selectivity, and thermal stability.<sup>4</sup> For example, copper oxides (CuO<sub>x</sub>) supported on Al<sub>2</sub>O<sub>3</sub>-based composite oxide materials (such as 10Al<sub>2</sub>O<sub>3</sub>·2B<sub>2</sub>O<sub>3</sub> and 3Al<sub>2</sub>O<sub>3</sub>·2SiO<sub>2</sub>) exhibit high N<sub>2</sub> selectivity and thermal stability, whereas binary CuO<sub>x</sub> and silver (Ag) supported on Al<sub>2</sub>O<sub>3</sub> exhibit high activity and N<sub>2</sub> selectivity.<sup>4</sup> However, the former catalyst exhibits a low activity (ignition temperature at ~300 °C), while the latter catalyst exhibits low thermal stability (deactivation temperature at ~900 °C likely because of the low melting point of Ag).<sup>4</sup> Therefore, it is imperative to develop catalysts to exhibit high activities and thermal stabilities for NH<sub>3</sub> combustion.

<sup>a</sup>Field of Environmental Chemistry and Materials, Division of Materials Science and Chemistry, Faculty of Advanced Science and Technology, Kumamoto University, 2-39-1 Kurokami, Chuo-ku, Kumamoto 860-8555, Japan. E-mail: hinokuma@kumamoto-u.ac.jp; Tel: +81-96-342-3653

<sup>b</sup>Department of Chemistry, Faculty of Science, Hokkaido University, Sapporo 060-0810, Japan

<sup>c</sup>International Research Organization for Advanced Science and Technology, Kumamoto University, Japan

† Electronic supplementary information (ESI) available: Calculation formulae, calculated thermodynamic Pt–PtO<sub>x</sub> phase equilibrium, XRD patterns, HAADF-STEM/EDX mapping images, product selectivities for the NH<sub>3</sub>–O<sub>2</sub> and NH<sub>3</sub>–NO–O<sub>2</sub> reactions, relationship between NH<sub>3</sub> combustion activity and Pt particle size, NH<sub>3</sub>- and NO-TPD profiles. See DOI: 10.1039/c8ra07969b



On the other hand, binary systems comprising supported  $\text{CuO}_x\text{-Ag}$ ,<sup>5</sup>  $\text{CuO}_x\text{-Pt}$ ,<sup>6</sup>  $\text{CuO}_x\text{-Au}$ ,<sup>7</sup>  $\text{CuO}_x\text{-CeO}_2$ <sup>8</sup> and  $\text{-Li}_2\text{O}_3$ <sup>8</sup> catalysts exhibiting a high performance for the selective catalytic oxidation of  $\text{NH}_3$  ( $\text{NH}_3\text{-SCO}$ ) have been previously reported. In particular,  $\text{CuO}_x\text{-Pt}$  systems are expected to exhibit high thermal stability because of the high melting point of Pt ( $\sim 1770^\circ\text{C}$ ). Recently, Sun *et al.* have synthesised impregnated  $\text{CuO}_x\text{-Pt/ZSM-5}$  catalysts and reported that  $\text{CuO}_x$  on Pt species can lead to higher  $\text{NH}_3\text{-SCO}$  performance compared to single catalysts.<sup>6</sup> On the other hand, Jabłońska has synthesised  $\text{Al}_2\text{O}_3$ -,  $\text{TiO}_2$ -, and  $\text{ZrO}_2$ -supported  $\text{CuO}_x\text{-Pt}$ ,  $\text{-Pd}$  and  $\text{-Rh}$  catalysts<sup>6</sup> and found that the supported  $\text{CuO}_x\text{-Pt}$  catalyst exhibits high activity and  $\text{N}_2$  selectivity for  $\text{NH}_3\text{-SCO}$ . However, in these studies,  $\text{NH}_3$  is considered to cause air pollution; therefore, the thermal stability is investigated at temperatures of less than  $900^\circ\text{C}$ .

In this study, supported binary  $\text{CuO}_x\text{-Pt}$  catalysts were synthesised, and their catalytic properties for the combustion of  $\text{NH}_3$  (as an energy source) at high reaction temperatures were examined. To achieve high catalytic activity for the combustion of  $\text{NH}_3$ ,  $\text{N}_2$  (low  $\text{N}_2\text{O/NO}$ ) selectivity and thermal stability, preparation conditions for impregnated binary catalysts were optimised. Moreover, the relationship between the local structure and catalytic properties for the combustion of  $\text{NH}_3$  over supported  $\text{CuO}_x\text{-Pt}$  catalysts was discussed.

## Experimental

### Catalyst preparation

$3\text{Al}_2\text{O}_3 \cdot 2\text{SiO}_2$  (3A2S) of the catalyst support material was prepared by using an alkoxide method. According to previous studies,<sup>4,9</sup>  $\text{Si}(\text{OC}_2\text{H}_5)_4$  (TEOS, Wako Pure Chemicals) was first dissolved in  $\text{C}_2\text{H}_5\text{OH}$  (Wako Pure Chemicals) at a concentration of 1 M at room temperature (RT). Second, after the addition of  $\text{H}_2\text{O}$  and  $\text{HCl}$  (Wako Pure Chemicals), the solution was stirred at  $70^\circ\text{C}$  for 5 h, and a Si solution was prepared. Third, the alcohol was dehydrated. The  $\text{H}_2\text{O}$  and  $\text{HCl}$  concentrations were  $\text{H}_2\text{O/TEOS} = 2$  ( $\text{mol mol}^{-1}$ ) and  $\text{HCl/TEOS} = 0.1$  ( $\text{mol mol}^{-1}$ ), respectively. Next,  $\text{Al}[\text{OCH}(\text{CH}_3)_2]_3$  (AIP, Sigma-Aldrich) was subjected to reflux conditions and dissolved in  $(\text{CH}_3)_2\text{-CHCH}_2\text{OH}$  (Nacalai Tesque) to prepare an Al solution. The precursor solution was prepared by mixing the Al and Si solutions in a volume ratio of 3 : 2 at RT.  $\text{H}_2\text{O}$  was added, and the solution was stirred for 1 h to prepare the precursor solution. The precursor sols were dried at  $110^\circ\text{C}$  for 48 h, affording xerogel precursor powders. These powders were pulverised and calcined at  $600^\circ\text{C}$  for 3 h and finally at  $1200^\circ\text{C}$  for 5 h in air. In addition,  $\alpha\text{-Al}_2\text{O}_3$  (Wako Pure Chemicals),  $\gamma\text{-Al}_2\text{O}_3$  (JRC-ALO-8, Catalysis Society of Japan),  $\text{SiO}_2$  (JRC-SIO-10, Catalysis Society of Japan), and  $\text{CuO}$  (Wako Pure Chemicals) were used as support materials.

Single and binary supported  $\text{CuO}_x$  ( $\text{CuO}$  loading of 6 wt%) and/or Pt (Pt loading of 2 wt%) catalysts were prepared by the co-impregnation ( $\text{CuO}_x\text{-Pt}$ ) of an aqueous solution of  $\text{Cu}(\text{NO}_3)_2$  (Wako Pure Chemicals) and  $[\text{Pt}(\text{NH}_3)_2(\text{NO}_3)_2]$  (Tanaka Kikinzoku Kogyo), followed by drying and calcination at  $600^\circ\text{C}$  for 3 h in air. In addition, the sequentially impregnated binary catalysts, *i.e.* Pt and subsequent  $\text{CuO}_x$  ( $\text{CuO}_x\text{/Pt}$ ) and/or  $\text{CuO}_x$  and

subsequent Pt ( $\text{Pt/CuO}_x$ ), were synthesised in a similar fashion. As  $\text{CuO}_x\text{/Pt/Al}_2\text{O}_3$  exhibited a high catalytic activity for the combustion of  $\text{NH}_3$ , physically mixed catalysts ( $\text{CuO} + \text{Pt/Al}_2\text{O}_3$ ,  $\text{CuAl}_2\text{O}_4 + \text{Pt/Al}_2\text{O}_3$ , and  $\text{CuO}_x\text{/Al}_2\text{O}_3 + \text{Pt/Al}_2\text{O}_3$ ) with the same composition ratios were also prepared. To evaluate their thermal stabilities and catalytic properties, the as-prepared catalysts were subjected to thermal aging at  $900^\circ\text{C}$  for 100 h in air and/or at  $1000^\circ\text{C}$  for 5 h in air.

### Characterisation

Powder X-ray diffraction (XRD) patterns were recorded using monochromatic  $\text{Cu K}\alpha$  radiation (30 kV, 20 mA, Multiflex, Rigaku). The average size of the Pt particles was calculated by the XRD line broadening method by using the Scherrer equation.<sup>10</sup> The chemical composition was determined by X-ray fluorescence (XRF; EDXL-300, Rigaku) measurements. High-angle annular dark-field scanning transmission electron microscopy (HAADF-STEM) and energy-dispersive X-ray spectroscopy (EDS) mapping images were recorded on a JEM-ARM200CF (JEOL) system. Brunauer-Emmett-Teller (BET) surface area ( $S_{\text{BET}}$ ) values were calculated from the  $\text{N}_2$  adsorption isotherms, which were recorded at  $-196^\circ\text{C}$  (Belsorp, Bel Japan, Inc.). Pt dispersion and particle size were determined by the pulsed CO technique (BELCAT-B, BEL Japan, Inc.) at  $50^\circ\text{C}$  after  $\text{O}_2$  oxidation and subsequent  $\text{H}_2$  reduction at  $400^\circ\text{C}$  according to previous studies.<sup>11</sup> Pt dispersion and particle size were calculated by assuming hemispherical particles with the stoichiometric adsorption of CO on Pt at a CO : Pt ratio of 1 : 1. Cu K-edge and Pt  $\text{L}_{3\text{-edge}}$  X-ray absorption fine structure (XAFS) spectral analyses were carried out at BL9A of PF and BL01B1 of SPring-8. XAFS spectra were recorded in the transmission mode at RT using an ionisation chamber filled with  $\text{N}_2$  for the incident beam, another chamber filled with 75%  $\text{N}_2/\text{Ar}$  for the Cu K-edge and 50%  $\text{N}_2/\text{Ar}$  for Pt  $\text{L}_{3\text{-edge}}$  for the transmitted beam, and a  $\text{Si}(111)$  double-crystal monochromator. Reference samples (*e.g.*  $\text{Cu}_2\text{O}$ ,  $\text{CuO}$ ,  $\text{CuAl}_2\text{O}_4$ , and  $\text{PtO}_2$ ) were mixed with boron nitride (BN) powder to achieve an appropriate absorbance at the edge energy, whereas the catalysts were used without mixing with BN. XAFS data were processed using the IFEFFIT software package (Athena and Artemis).

### Catalytic $\text{NH}_3$ combustion tests

The catalytic combustion of  $\text{NH}_3$  was performed in a flow reactor at atmospheric pressure. Catalysts (10–20 mesh,  $<0.3$  mm thickness, 50 mg) were fixed in a quartz tube (OD: 6 mm, ID: 4 mm) with quartz wool at both ends of the catalyst bed. The temperature dependence of the catalytic activity was evaluated by heating the catalyst bed from RT to  $900^\circ\text{C}$  at a constant rate of  $10^\circ\text{C min}^{-1}$  while a gas mixture containing 1.0%  $\text{NH}_3$ , 1.5%  $\text{O}_2$  and He balance at  $100\text{ cm}^3\text{ min}^{-1}$  ( $W/F = 5.0 \times 10^{-4}\text{ g min cm}^{-3}$ ) was supplied. The  $\text{O}_2$  excess ratio for  $\text{NH}_3$  combustion was expressed as  $\lambda = (p_{\text{O}_2}/p_{\text{NH}_3})_{\text{exp}}/(p_{\text{O}_2}/p_{\text{NH}_3})_{\text{stoichiom.}}$ , where  $p$  denotes pressure. The  $\text{NH}_3/\text{N}_2\text{O/NO}$ ,  $\text{N}_2$  and  $\text{NO}_2$  gas concentrations were analysed using a nondispersive infrared gas analyser (VA-3011, Horiba), chromatography (GC-8A, Shimadzu) and chemiluminescence (NOA-7000,



Shimadzu) measurements. The ESI† provides the calculation formulae used to determine the concentration ratios.

*In situ* Fourier transform infrared (FTIR) spectra were recorded on a Nicolet 6700 spectrometer using a diffuse-reflectance reaction cell with a BaF<sub>2</sub> window connected to a gas supply and a heating system to enable measurements at atmospheric pressure. First, the catalysts were preheated *in situ* in flowing He at 400 °C for 30 min prior to each experiment. After pre-treatment, the temperature of the catalyst was decreased to 200 °C, followed by the subsequent purging of the cell with He and then filling with 0.3% NH<sub>3</sub>/He mixed gas. Finally, FTIR spectra were recorded while the catalysts were maintained under a stream of NH<sub>3</sub>/He.

### Computational details

Spin-restricted density functional theory (DFT) computations were carried out for NH<sub>3</sub>/Pt<sub>x</sub> ( $x = 13$  and/or  $20$ ) at the M06 level using the def-SV(P) basis sets, with the 60-electron relativistic effective core potential for Pt, as implemented in TURBOMOLE under the resolution of the identity approximation.<sup>12</sup> The model clusters of Pt<sub>13</sub> with *I*<sub>h</sub> symmetry and Pt<sub>20</sub> with *T*<sub>d</sub> symmetry having four (111) faces were locally optimised until imaginary frequencies were removed. One atop geometry for NH<sub>3</sub>-Pt<sub>13</sub> and three initial geometries for NH<sub>3</sub>-Pt<sub>20</sub> were considered, *i.e.* atop the (111) face; bridge-to-edge site; and atop the vertex site, respectively. These geometries were optimised until no imaginary frequencies were observed. The adsorption energy of NH<sub>3</sub> on Pt<sub>x</sub> was estimated as  $E_{\text{ads}} = E(\text{NH}_3) + E(\text{Pt}_x) - E(\text{NH}_3\text{-Pt}_x)$ , where  $E(A)$  denotes the electronic energy of species *A*.

## Results & discussion

### Local structures of supported CuO<sub>x</sub> and Pt catalysts

Fig. 1 shows the XRD patterns of sequentially impregnated binary (CuO<sub>x</sub>/Pt) catalysts, because CuO<sub>x</sub>/Pt/Al<sub>2</sub>O<sub>3</sub> exhibited

higher activity, N<sub>2</sub> (lower N<sub>2</sub>O/NO) selectivity, and thermal stability for the combustion of NH<sub>3</sub> compared to all binary catalysts before and after thermal ageing at 900 °C (Table 1). ESI† shows the XRD patterns of the other catalysts. The XRD patterns of as-prepared CuO<sub>x</sub>/Pt/3A2S and CuO<sub>x</sub>/Pt/SiO<sub>2</sub> before and after aging revealed peaks corresponding to CuO, whereas peaks corresponding to CuAl<sub>2</sub>O<sub>4</sub> were observed for CuO<sub>x</sub>/Pt/3A2S and CuO<sub>x</sub>/Pt/Al<sub>2</sub>O<sub>3</sub> (900 °C), possibly related to the solid-state reaction between  $\gamma$ -Al<sub>2</sub>O<sub>3</sub> and CuO<sub>x</sub>. Diffraction peaks for Cu species were not observed for as-prepared CuO<sub>x</sub>/Pt/Al<sub>2</sub>O<sub>3</sub>, possibly related to the high dispersion of CuO<sub>x</sub>. The Al<sub>2</sub>O<sub>3</sub> phase for the binary catalysts was transformed from  $\gamma$  to  $\alpha$ , and the diffraction peaks for Pt became sharper after thermal aging at temperatures of higher than 900 °C. Therefore, the growth of particles and sintering of Al<sub>2</sub>O<sub>3</sub> and Pt are induced by thermal aging. Indeed, the Pt particle sizes calculated by the Scherrer equation increased with the aging temperature (Table 1). On the other hand, as peaks corresponding to CuO were observed for the binary catalysts prepared using  $\alpha$ -Al<sub>2</sub>O<sub>3</sub> (CuO<sub>x</sub>/Pt/ $\alpha$ -Al<sub>2</sub>O<sub>3</sub>) before and after aging, it was possibly difficult to form CuAl<sub>2</sub>O<sub>4</sub> from the solid-state reaction between  $\alpha$ -Al<sub>2</sub>O<sub>3</sub> and CuO<sub>x</sub> (ESI†).

Fig. 2 shows the normalised Cu K-edge X-ray absorption near-edge structure (XANES) spectra and *k*-space extended X-ray absorption fine structure (EXAFS) oscillations of the catalysts and the three reference compounds (Cu<sub>2</sub>O, CuO and CuAl<sub>2</sub>O<sub>4</sub>, respectively). Cu K-edge XANES spectra and *k*-space EXAFS oscillations of CuO<sub>x</sub>/Pt/3A2S (900 °C) and CuO<sub>x</sub>/Pt/Al<sub>2</sub>O<sub>3</sub> before and after thermal aging at 900 °C were similar to those of CuAl<sub>2</sub>O<sub>4</sub>, whereas those of CuO<sub>x</sub>/Pt/3A2S and CuO<sub>x</sub>/Pt/SiO<sub>2</sub> before and after thermal aging at 900 °C were similar to those of CuO. In the XANES spectra of CuO<sub>x</sub>/Pt/3A2S and CuO<sub>x</sub>/Pt/SiO<sub>2</sub> before and after aging, the pre-edge (at ~8985 eV, corresponding to Cu<sup>2+</sup> 1s → 4p + ligand and Cu<sup>2+</sup> 1s → Cu<sup>2+</sup> charge-transfer excitation)<sup>13</sup> for CuO was observed. XAFS analyses were consistent with the XRD patterns of the catalysts. The Pt L<sub>3</sub>-edge XAFS profiles of the catalysts and two references (*i.e.* Pt foil and PtO<sub>2</sub>, respectively) are also depicted in Fig. 3. For as-prepared CuO<sub>x</sub>/Pt/Al<sub>2</sub>O<sub>3</sub>, the XANES profile was slightly similar to that observed for PtO<sub>2</sub>. According to the calculated thermodynamic Pt-PtO<sub>x</sub> phase equilibrium (ESI†), PtO<sub>2</sub> and metallic Pt exhibited thermodynamic stability at RT and 600 °C, respectively. Therefore, Pt nanoparticles (especially, their surfaces) in CuO<sub>x</sub>/Pt/Al<sub>2</sub>O<sub>3</sub> are thought to be oxidised during the cooling process of calcination. By contrast, the XANES profiles of the other catalysts were similar to that of Pt foil (metallic Pt) as against the calculated phase equilibrium. This disagreement is supposedly caused by the calcination and/or thermal aging-induced sintering of metallic Pt nanoparticles in these catalysts; hence, the bulk metallic Pt particles are stable at RT.

Next, HAADF-STEM and EDS mapping images of sequentially impregnated CuO<sub>x</sub>/Pt/Al<sub>2</sub>O<sub>3</sub> (900 °C) were recorded (Fig. 4). From the HAADF-STEM image, dispersed nanoparticles with a bright contrast supported on Al<sub>2</sub>O<sub>3</sub> particles (blue for Al) were observed, and the EDS mapping images revealed the presence of Pt (red). On the other hand, for the CuO<sub>x</sub> species of CuO<sub>x</sub>/Pt/Al<sub>2</sub>O<sub>3</sub> (900 °C), the EDS mapping images revealed the presence of CuO<sub>x</sub> aggregates (green). However, because the

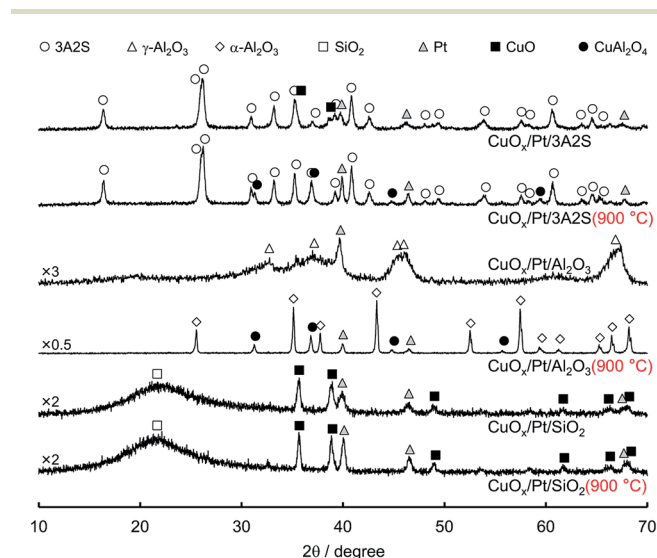


Fig. 1 XRD patterns of sequentially impregnated catalysts before and after thermal aging 900 °C for 100 h in air.



Table 1 Catalytic properties of supported catalysts before and after thermal aging at 900 °C for 100 h in air

Catalyst	Phase	$T_{10}^a/^\circ\text{C}$	$T_{90}^a/^\circ\text{C}$	Selectivity at $T_{90}^a/\%$			$S_{\text{BET}}/\text{m}^2\text{ g}^{-1}$	Pt particle size/nm		Desorbed gas <sup>d</sup> /μmol m <sup>-2</sup>	
				N <sub>2</sub>	N <sub>2</sub> O	NO		<sup>b</sup> XRD	<sup>c</sup> Pulsed CO	NH <sub>3</sub>	NO
CuO <sub>x</sub> /Pt/3A2S	CuO/Pt/3A2S	210	356	90	8	2	32		18		
CuO <sub>x</sub> /Pt/3A2S (900 °C)	CuAl <sub>2</sub> O <sub>4</sub> /Pt/3A2S	203	344	89	10	1	27		50		
CuO <sub>x</sub> /Al <sub>2</sub> O <sub>3</sub>	CuAl <sub>2</sub> O <sub>4</sub> /γ-Al <sub>2</sub> O <sub>3</sub>	303	476	92	6	2	149			1.3	0.050
CuO <sub>x</sub> /Al <sub>2</sub> O <sub>3</sub> (900 °C)	CuAl <sub>2</sub> O <sub>4</sub> /α, γ-Al <sub>2</sub> O <sub>3</sub>	295	450	91	8	1	102			0.4	0.063
Pt/Al <sub>2</sub> O <sub>3</sub>	Pt/γ-Al <sub>2</sub> O <sub>3</sub>	188	289	81	19	<1	156	11	11	0.6	0.051
Pt/Al <sub>2</sub> O <sub>3</sub> (900 °C)	Pt/γ, θ-Al <sub>2</sub> O <sub>3</sub>	213	266	87	12	<1	99	31	<sup>e</sup> n. d.	2.0	0.140
CuO <sub>x</sub> /Pt/Al <sub>2</sub> O <sub>3</sub>	CuAl <sub>2</sub> O <sub>4</sub> /Pt/γ-Al <sub>2</sub> O <sub>3</sub>	189	278	86	13	<1	139	15	5	1.6	0.064
CuO <sub>x</sub> /Pt/Al <sub>2</sub> O <sub>3</sub> (900 °C)	CuAl <sub>2</sub> O <sub>4</sub> /Pt/α-Al <sub>2</sub> O <sub>3</sub>	220	339	86	13	1	14	33	176	1.5	0.444
CuO <sub>x</sub> /Pt/SiO <sub>2</sub>	CuO/Pt/SiO <sub>2</sub>	234	316	93	7	<1	182	13	<sup>e</sup> n. d.		
CuO <sub>x</sub> /Pt/SiO <sub>2</sub> (900 °C)	CuO/Pt/SiO <sub>2</sub>	301	456	96	<1	3	81	24	<sup>e</sup> n. d.		

<sup>a</sup> Temperature at which NH<sub>3</sub> conversion reached 10% and 90%. <sup>b</sup> Calculated from XRD line broadening method. <sup>c</sup> Calculated from pulsed CO chemisorption. <sup>d</sup> Estimated by NH<sub>3</sub>- and NO-TPD ranging from 50 °C to 500 °C. <sup>e</sup> The amount of CO chemisorption was not detected (n. d.).

overlap of the fluorescence lines of Pt-L and Cu-K, as denoted by the solid arrows in the overlaid image, a physical proximity between Pt and CuO<sub>x</sub> nanoparticles in CuO<sub>x</sub>/Pt/Al<sub>2</sub>O<sub>3</sub> was supposed after aging at 900 °C. On the other hand, Pt particles with sizes larger than 200 nm were clearly observed for CuO<sub>x</sub>/Pt/SiO<sub>2</sub> (900 °C) (ESI†).

### Combustion properties of supported CuO<sub>x</sub> and Pt catalysts

Fig. 5 shows the comparison of the temperature dependence on the selectivities of products obtained over supported CuO<sub>x</sub>/Pt, CuO<sub>x</sub>/Al<sub>2</sub>O<sub>3</sub> and Pt/Al<sub>2</sub>O<sub>3</sub> before and after thermal aging at 900 °C under O<sub>2</sub> excess conditions ( $\lambda = 2$ ). ESI† shows those of the other catalysts. With respect to the supported CuO<sub>x</sub>/Pt catalysts before and after aging, CuO<sub>x</sub>/Pt/Al<sub>2</sub>O<sub>3</sub> exhibited a comparatively higher catalytic NH<sub>3</sub> combustion activity and N<sub>2</sub> (lower N<sub>2</sub>O/NO) selectivity. For CuO<sub>x</sub>/Pt/Al<sub>2</sub>O<sub>3</sub> and Pt/Al<sub>2</sub>O<sub>3</sub> before and after aging, the light-off curves for NH<sub>3</sub> were obtained at ~200 °C, whereas CuO<sub>x</sub>/Al<sub>2</sub>O<sub>3</sub> exhibited lower catalytic activity ( $T_{10}$ : ~300 °C). On the other hand, before and after aging, CuO<sub>x</sub>/Pt/Al<sub>2</sub>O<sub>3</sub> and CuO<sub>x</sub>/Al<sub>2</sub>O<sub>3</sub> exhibited lower NO selectivity compared to Pt/Al<sub>2</sub>O<sub>3</sub> although NO selectivities for all catalysts were observed after the NH<sub>3</sub> conversion reached ~90%. In contrast, the selectivity of N<sub>2</sub>O over the catalysts before and after aging increased in the order of CuO<sub>x</sub>/Al<sub>2</sub>O<sub>3</sub> < CuO<sub>x</sub>/Pt/Al<sub>2</sub>O<sub>3</sub> < Pt/Al<sub>2</sub>O<sub>3</sub>. Finally, CuO<sub>x</sub>/Pt/Al<sub>2</sub>O<sub>3</sub> exhibited higher N<sub>2</sub> selectivity. Therefore, binary CuO<sub>x</sub>/Pt/Al<sub>2</sub>O<sub>3</sub> renders synergistic effects of Pt (enhancing the NH<sub>3</sub>-O<sub>2</sub> reaction) and CuO<sub>x</sub> (increasing N<sub>2</sub> selectivity). To investigate the low NO selectivity of CuO<sub>x</sub>/Pt/Al<sub>2</sub>O<sub>3</sub> and CuO<sub>x</sub>/Al<sub>2</sub>O<sub>3</sub>, an NH<sub>3</sub>-NO-O<sub>2</sub> reaction test (0.8% NH<sub>3</sub>, 0.2% NO, 1.4% O<sub>2</sub>, He balance) was also performed (shown in ESI†). For the NH<sub>3</sub>-NO reaction, CuO<sub>x</sub>/Pt/Al<sub>2</sub>O<sub>3</sub> also exhibited higher activity compared to CuO<sub>x</sub>/Al<sub>2</sub>O<sub>3</sub> and Pt/Al<sub>2</sub>O<sub>3</sub>. NH<sub>3</sub> was supposedly consumed not only by O<sub>2</sub> but also by NO, which was formed as an intermediate during the light-off of NH<sub>3</sub>. However, the selectivity of N<sub>2</sub>O for the NH<sub>3</sub>-NO-O<sub>2</sub> reaction over CuO<sub>x</sub>/Pt/Al<sub>2</sub>O<sub>3</sub> was higher than that for the

combustion of NH<sub>3</sub> (Fig. 5), indicating that the N<sub>2</sub>O is produced from the NH<sub>3</sub>-NO reaction.

For N<sub>2</sub>O production, on the other hand, according to the kinetic model for NH<sub>3</sub> oxidation, the elementary reaction of NH (imide) + NO → N<sub>2</sub>O + H exhibited high sensitivity for N<sub>2</sub>O production.<sup>14</sup> Moreover, for catalytic NH<sub>3</sub> oxidation and NH<sub>3</sub>-NO reactions, NH was also regarded as a key species for N<sub>2</sub>O production.<sup>15</sup> Therefore, to verify the adsorption of NH on the catalysts, *in situ* FTIR spectra of NH<sub>3</sub> adsorbed on the catalysts before and after aging were recorded at 200 °C (Fig. 6); this temperature is the approximate initiation temperature for NH<sub>3</sub> combustion (Fig. 5). As has been reported previously,<sup>15</sup> FTIR bands were observed at 1250 and 1625 cm<sup>-1</sup>, corresponding to the deformation modes of NH<sub>3</sub> adsorbed on Lewis acid sites, for all catalysts. Moreover, for Pt/Al<sub>2</sub>O<sub>3</sub> and CuO<sub>x</sub>/Pt/Al<sub>2</sub>O<sub>3</sub>, a set of bands were slightly observed at 1395 and 1695 cm<sup>-1</sup>, corresponding to the asymmetric and symmetric bending vibrations of NH<sub>3</sub> species on the Brønsted acid sites. Although the single band at 1458 cm<sup>-1</sup> corresponding to the NH (considered as a species for N<sub>2</sub>O production) deformation modes was observed for all catalysts, the band intensity for CuO<sub>x</sub>/Pt/Al<sub>2</sub>O<sub>3</sub> was less than that for Pt/Al<sub>2</sub>O<sub>3</sub>. As CuO<sub>x</sub>/Pt/Al<sub>2</sub>O<sub>3</sub> prevented the production of NO from the combustion of NH<sub>3</sub> and the dissociative adsorption of NH<sub>3</sub>, the catalyst finally achieved high N<sub>2</sub> selectivity.

### Catalytic properties of supported CuO<sub>x</sub> and/or Pt

Table 1 summarises the catalytic properties of supported CuO<sub>x</sub>/Pt, CuO<sub>x</sub>/Al<sub>2</sub>O<sub>3</sub> and Pt/Al<sub>2</sub>O<sub>3</sub> before and after thermal aging at 900 °C, and ESI† shows those of the other catalysts. Catalytic activity was expressed in terms of the light-off temperature at which 10% conversion of NH<sub>3</sub> was achieved ( $T_{10}$ ), and the product selectivities were evaluated at the reaction temperature at which 90% NH<sub>3</sub> conversion was achieved ( $T_{90}$ ). ESI† shows the temperature dependence of the product selectivities for the combustion of NH<sub>3</sub> over the catalysts. For single catalysts supported on each material (*i.e.* 3A2S, Al<sub>2</sub>O<sub>3</sub> and SiO<sub>2</sub>), supported





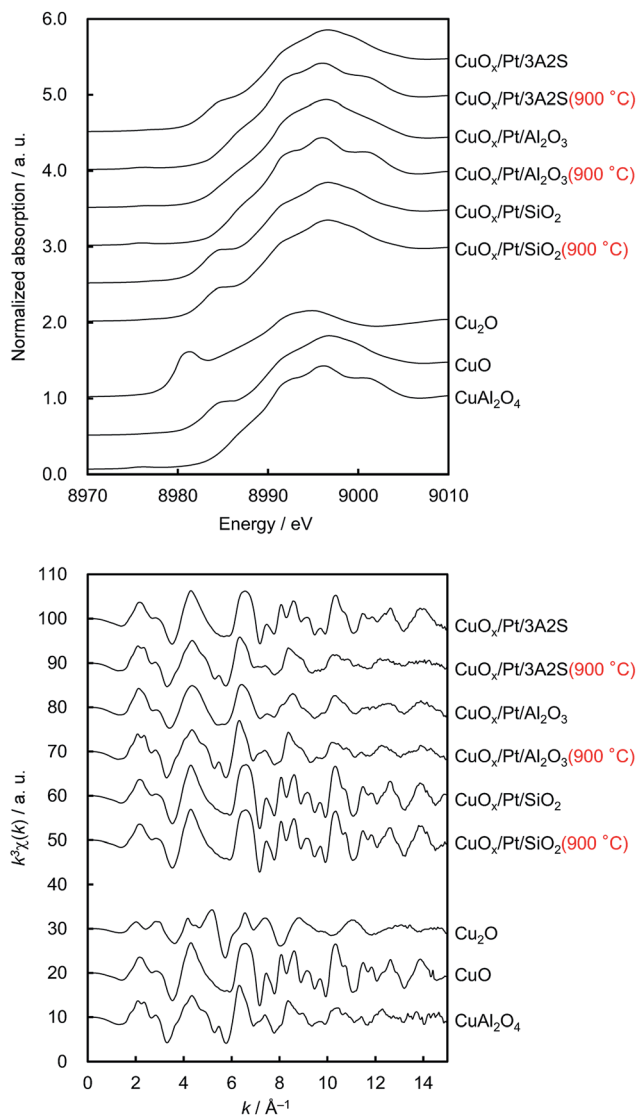


Fig. 2 Cu K-edge (upper) normalised XANES spectra and (lower) EXAFS oscillations of sequentially impregnated catalysts before and after thermal aging and three references (i.e.  $\text{Cu}_2\text{O}$ ,  $\text{CuO}$ , and  $\text{CuAl}_2\text{O}_4$ , respectively).

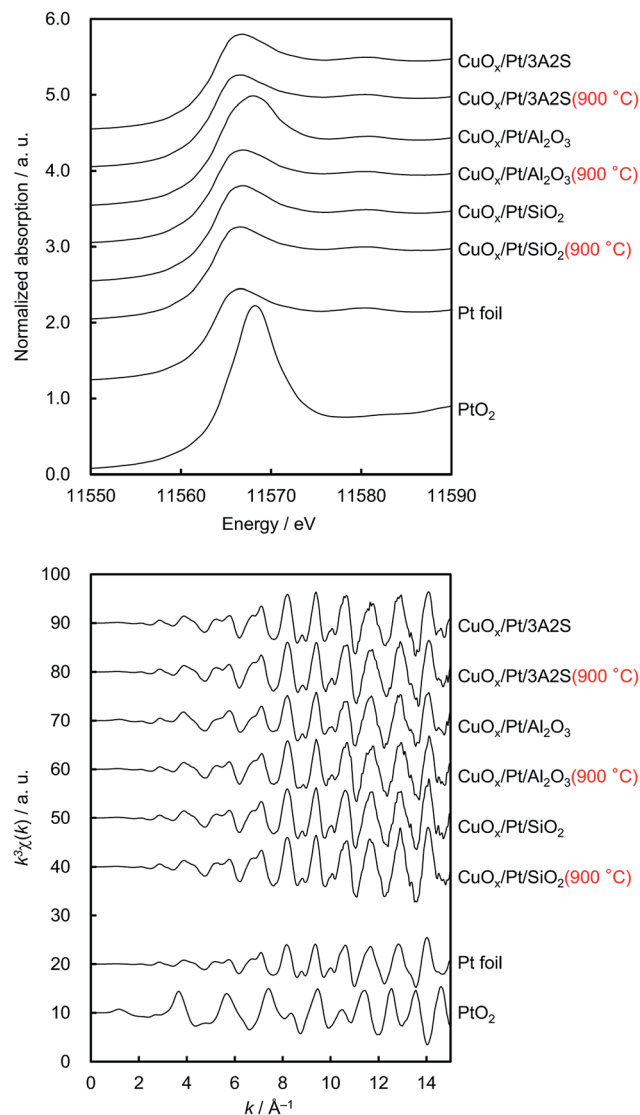


Fig. 3 Pt  $L_3$ -edge (upper) normalised XANES spectra and (lower) EXAFS oscillations of sequentially impregnated catalysts before and after thermal aging and two references (i.e. Pt foil and  $\text{PtO}_2$ , respectively).

$\text{CuO}_x$  exhibited low activity and  $\text{N}_2\text{O}/\text{NO}$  selectivities, whereas supported Pt exhibited high activity and  $\text{N}_2\text{O}/\text{NO}$  selectivity ( $\text{ESI}^\dagger$ ). On the other hand, binary supported catalysts exhibited the same high activity as the single supported Pt, albeit a slightly lower  $\text{N}_2\text{O}/\text{NO}$  selectivity. As the combustion activity was closely associated with the Pt particle size, which was calculated by the Scherrer equation (plot shown in the  $\text{ESI}^\dagger$ ), highly dispersed Pt nanoparticles supposedly played a key role in the low-temperature light-off of  $\text{NH}_3$ . In this study, for pulsed CO chemisorption, it is expected that CO is adsorbed not only on Pt but also on  $\text{CuO}_x$  in case of binary system catalysts.<sup>16</sup> Therefore, the correlation between the  $\text{NH}_3$  combustion activity ( $T_{10}$ ) and the Pt particle size can be estimated using the XRD line broadening method by employing the Scherrer equation.

To elucidate the correlation between the activity and size of Pt nanoparticles, the adsorption energy ( $E_{\text{ads}}$ ) between  $\text{NH}_3$  and  $\text{Pt}_{13}$  and/or  $\text{Pt}_{20}$  clusters (Pt–N) were estimated by DFT computations (Fig. 7). Compared with the Pt–N  $E_{\text{ads}}$  of the vertex for the  $\text{Pt}_{20}$  (larger) cluster, that of the vertex for the  $\text{Pt}_{13}$  (smaller) cluster was higher, indicating that  $\text{NH}_3$  preferentially adsorbs on highly dispersed Pt nanoparticles as well as coordinatively unsaturated (cus) Pt atoms. Indeed, for the  $\text{Pt}_{20}$  cluster, the Pt–N  $E_{\text{ads}}$  of three initial geometries (see inset in Fig. 7) increased in the order of atop < edge < vertex. Moreover, the bond distance of N–H in  $\text{NH}_3$  adsorbed on  $\text{Pt}_{13}$  was longer than that on  $\text{Pt}_{20}$ , suggesting that cus Pt exhibits high activity for the dissociation of the N–H bond in adsorbed  $\text{NH}_3$ . Compared with the activity of binary  $\text{CuO}_x$ –Pt catalysts prepared by co-impregnation, those of the sequentially impregnated  $\text{CuO}_x$ /Pt catalysts were higher



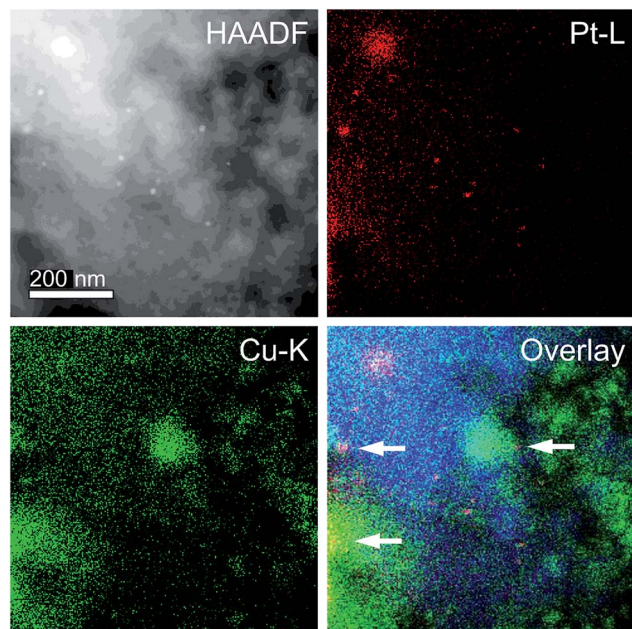


Fig. 4 HAADF-STEM image and EDS mapping analysis of  $\text{CuO}_x/\text{Pt}/\text{Al}_2\text{O}_3$  (900 °C). Red, green, and blue points denote the Pt-L, Cu-K, and Al-K fluorescence lines, respectively.

probably because Pt nanoparticles can be highly dispersed onto each support material without inhibition from the presence of  $\text{CuO}_x$ .

Among the  $\text{CuO}_x/\text{Pt}$  catalysts supported on various support materials,  $\text{CuO}_x/\text{Pt}/\text{Al}_2\text{O}_3$  exhibited a relatively higher activity,  $\text{N}_2$  selectivity, and thermal stability (Table 1). However, a significant decrease in  $S_{\text{BET}}$  was observed for  $\text{CuO}_x/\text{Pt}/\text{Al}_2\text{O}_3$  (900 °C) ( $139 \rightarrow 14 \text{ m}^2 \text{ g}^{-1}$ ) in comparison with that observed for  $\text{CuO}_x/\text{Al}_2\text{O}_3$  (900 °C) and  $\text{Pt}/\text{Al}_2\text{O}_3$  (900 °C). For this reason, first, it is considered that the significant decrease in specific surface area can be attributed to the phase transition of ( $\gamma \rightarrow \alpha$ )  $\text{Al}_2\text{O}_3$  as well as thermal aging at 900 °C. However, in case of only  $\gamma\text{-Al}_2\text{O}_3$ , the phase transformation to  $\alpha\text{-Al}_2\text{O}_3$  was observed at approximately 1200 °C.<sup>17</sup> Next, however, according to a previous report related to the effects of divalent cation additives on the phase transition of ( $\gamma \rightarrow \alpha$ )  $\text{Al}_2\text{O}_3$ , the additive  $\text{Cu}^{2+}$  species that coexist with  $\gamma\text{-Al}_2\text{O}_3$  accelerates its phase transition to  $\alpha\text{-Al}_2\text{O}_3$  at a low temperature of 1200 °C, which can be attributed to the fact that  $\text{CuAl}_2\text{O}_4$  is formed at a temperature of lower than 1200 °C.<sup>18</sup> Indeed, in this study,  $\alpha\text{-Al}_2\text{O}_3$  was observed in  $\text{CuO}_x/\text{Al}_2\text{O}_3$  after thermal aging at 900 °C (Table 1). Finally, it is probable that the additive and co-existing Pt also accelerates the formation of  $\text{CuAl}_2\text{O}_4$  as well as the phase transition to  $\alpha\text{-Al}_2\text{O}_3$ . Although no concrete data are available, a similar significant decrease of the specific surface area could be observed in both Cu–Al–O and Cu–Pt–Al–O system catalysts after thermal aging occurred at 1000 °C.<sup>19</sup>

Notably, the high performance for  $\text{CuO}_x/\text{Pt}/\text{Al}_2\text{O}_3$  was maintained after thermal aging at 1000 °C despite the phase transition ( $\gamma \rightarrow \alpha$ ) and decrease in the surface area. On the other hand,  $\text{CuO}_x/\text{Pt}$  supported on  $\alpha\text{-Al}_2\text{O}_3$  exhibited slightly higher  $\text{N}_2\text{O}/\text{NO}$

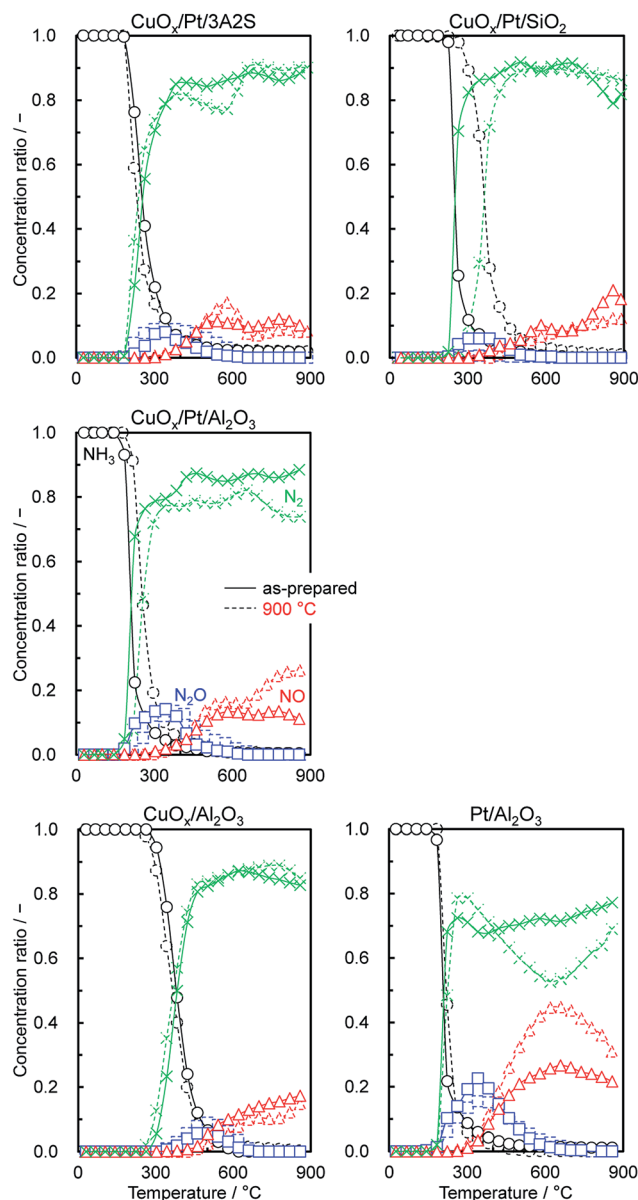


Fig. 5 Product selectivities for the catalytic combustion of  $\text{NH}_3$  ( $\text{NH}_3\text{-O}_2$ ) over catalysts before and after thermal aging in air at 900 °C for 100 h. Reaction conditions: 1.0%  $\text{NH}_3$ , 1.5%  $\text{O}_2$ ,  $\lambda = 2$ , He balance,  $W/F = 5.0 \times 10^{-4} \text{ g min cm}^{-3}$ .

selectivities compared to  $\text{CuO}_x/\text{Pt}/\text{Al}_2\text{O}_3$  (using  $\gamma\text{-Al}_2\text{O}_3$ ), the results of which can be explained from the difference in the  $\text{CuO}_x$  phase of  $\text{CuO}$  in  $\text{CuO}_x/\text{Pt}/\alpha\text{-Al}_2\text{O}_3$  and  $\text{CuAl}_2\text{O}_4$  in  $\text{CuO}_x/\text{Pt}/\gamma\text{-Al}_2\text{O}_3$ . Previously, our group has reported that supported  $\text{CuAl}_2\text{O}_4$  exhibits a higher  $\text{NH}_3\text{-NO-O}_2$  reaction activity to  $\text{N}_2$  compared to supported  $\text{CuO}$  because supported  $\text{CuAl}_2\text{O}_4$  exhibits a higher fraction of the  $\text{Cu}^{2+}$  active species for the reaction.<sup>4</sup> Therefore, the trend for  $\text{N}_2\text{O}/\text{NO}$  selectivities over  $\text{CuO}_x/\text{Pt}/\alpha\text{-Al}_2\text{O}_3$  and  $\text{CuO}_x/\text{Pt}/\text{Al}_2\text{O}_3$  can be explained in a similar manner. Moreover, physically mixed catalysts ( $\text{CuO} + \text{Pt}/\text{Al}_2\text{O}_3$ ,  $\text{CuAl}_2\text{O}_4 + \text{Pt}/\text{Al}_2\text{O}_3$  and  $\text{CuO}_x/\text{Pt}/\text{Al}_2\text{O}_3 + \text{Pt}/\text{Al}_2\text{O}_3$ ) exhibited lower  $\text{N}_2$  selectivity at high reaction temperatures (*ca.* > 600 °C) compared to binary catalysts ( $\text{ESI}^\dagger$ ), indicating that highly dispersed Pt and proximate  $\text{CuO}_x$  particles



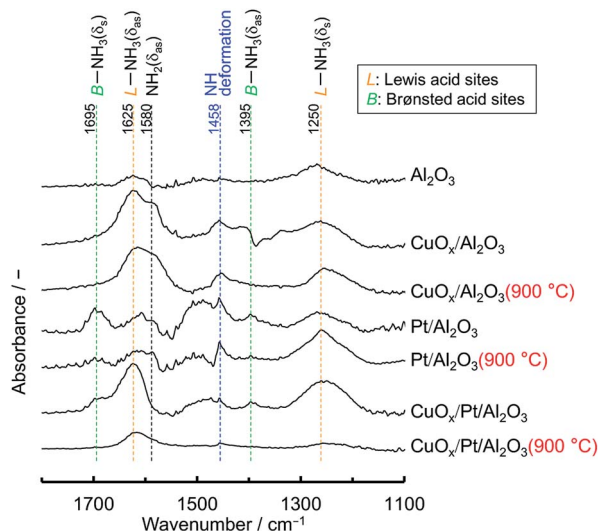


Fig. 6 *In situ* FTIR spectra of  $\text{NH}_3$  adsorbed on supports and catalysts before and after thermal aging in air at 900 °C for 100 h. The spectra were recorded at 200 °C in gas feeds of 0.3%  $\text{NH}_3$  with He balance.

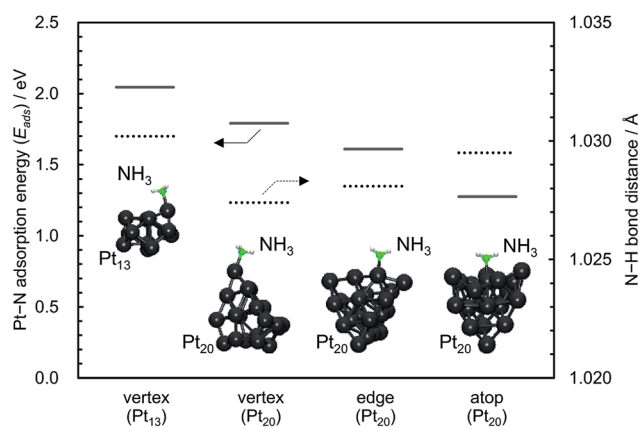


Fig. 7 Adsorption energy ( $E_{\text{ads}}$ ) between  $\text{NH}_3$  and  $\text{Pt}_{13}$  and/or  $\text{Pt}_{20}$  clusters (Pt-N) and bond distances of N-H in  $\text{NH}_3$  adsorbed on  $\text{Pt}_{13}$  and/or  $\text{Pt}_{20}$  obtained by the DFT computations.

are required to achieve high  $\text{N}_2$  selectivity for catalytic  $\text{NH}_3$  combustion. On the other hand,  $\text{Pt}/\text{CuO}$  exhibited high  $\text{N}_2$  selectivity, albeit low catalytic activity (ESI†), probably because of low Pt dispersion. To examine the acid and base properties of these catalysts, the amount of desorbed gas per surface area of the catalyst was estimated using  $\text{NH}_3$ - and  $\text{NO}$ -temperature-programmed desorption (TPD) over a range of 50–500 °C (ESI†). Table 1 summarises this data. For all catalysts after aging, the amount of desorbed  $\text{NO}$  increased noticeably, likely because of decreased surface area. However, before and after aging,  $\text{CuO}_x/\text{Pt}/\text{Al}_2\text{O}_3$  exhibited relatively higher  $\text{NH}_3$  and  $\text{NO}$  adsorption properties compared to  $\text{CuO}/\text{Al}_2\text{O}_3$  and  $\text{Pt}/\text{Al}_2\text{O}_3$ . These results indicated that  $\text{CuO}_x/\text{Pt}/\text{Al}_2\text{O}_3$  exhibits higher acidity and basicity compared to single supported catalysts; therefore, the reactivity of  $\text{NH}_3$ - $\text{NO}$  to  $\text{N}_2$  is enhanced on the  $\text{CuO}_x/\text{Pt}/\text{Al}_2\text{O}_3$  surface.

Finally, the effects of  $\text{CuO}$ ,  $\text{Cu}_2\text{O}$  and metallic  $\text{Cu}$  on the catalytic  $\text{NH}_3$  combustion properties are discussed. ESI† denotes

the comparison of the temperature dependence on the selectivities of the products that were obtained when compared to those of the commercially available  $\text{CuO}$ ,  $\text{Cu}_2\text{O}$  and metallic  $\text{Cu}$ . The metallic  $\text{Cu}$  was prepared from  $\text{CuO}$  that was reduced at 400 °C for 30 min in 5%  $\text{H}_2/\text{He}$  because  $\text{CuO}$  can be reduced to metallic  $\text{Cu}$  at an approximate temperature of 300 °C, as demonstrated from the  $\text{H}_2$ -TPR measurement.<sup>4</sup> For observing the  $\text{NH}_3$  combustion activity, the light-off curve for  $\text{CuO}$  was obtained at approximately 300 °C; further,  $\text{Cu}_2\text{O}$  and metallic  $\text{Cu}$  exhibited lower activity when compared to that exhibited by  $\text{CuO}$ . Therefore, it can be considered that  $\text{CuO}$  ( $\text{Cu}^{2+}$  oxidation state) acts as an active site during the reaction. However, while considering the selectivities of the products,  $\text{Cu}_2\text{O}$  and metallic  $\text{Cu}$  exhibited low  $\text{N}_2\text{O}/\text{NO}$  selectivities because their activities ( $\text{NH}_3$  conversions) were observed to be low. In the  $\text{O}_2$ -excess condition for  $\text{NH}_3$  combustion ( $\lambda = 2.0$ ), it can be considered that the combustion over  $\text{CuO}_x$  catalysts proceeds because of redox cycling between  $\text{CuO}$  and  $\text{Cu}_2\text{O}$ .<sup>4</sup> Further, the XRD patterns of  $\text{CuO}$  and  $\text{Cu}_2\text{O}$  before and after the reaction ( $\lambda = 2.0$ ) also indicate redox cycling because the patterns of  $\text{Cu}_2\text{O}$  after the reaction revealed diffraction peaks corresponding to those of  $\text{CuO}$  (ESI†). In addition, based on our previous studies related to *operando* XAFS, similar redox behaviours could be observed in the supported  $\text{CuO}$  catalysts ( $\text{CuO}_x/\text{SiO}_2$ ).<sup>4</sup> Therefore, it can be assumed that the effect of metallic  $\text{Cu}$  on combustion is negligible.

## Conclusions

In this study, binary  $\text{CuO}_x$  and  $\text{Pt}$  catalysts supported on 3A2S,  $\text{Al}_2\text{O}_3$  and  $\text{SiO}_2$  suppressed the production of  $\text{N}_2\text{O}/\text{NO}_x$  via the catalytic combustion of  $\text{NH}_3$  as a carbon-free energy source. Among the binary supported  $\text{CuO}_x$  and  $\text{Pt}$  catalysts, sequentially impregnated  $\text{CuO}_x/\text{Pt}$  catalysts tended to exhibit higher activity because  $\text{Pt}$  nanoparticles were highly dispersed onto each support material without inhibition due to the presence of  $\text{CuO}_x$ . Compared to sequentially impregnated  $\text{CuO}_x/\text{Pt}/3\text{A2S}$  and  $\text{CuO}_x/\text{Pt}/\text{SiO}_2$ ,  $\text{CuO}_x/\text{Pt}/\text{Al}_2\text{O}_3$  exhibited high  $\text{NH}_3$  combustion activity,  $\text{N}_2$  selectivity, and thermal stability. Before and after aging,  $\text{CuO}_x/\text{Pt}/\text{Al}_2\text{O}_3$  was characterised as proximate  $\text{CuAl}_2\text{O}_4$  and dispersed metallic  $\text{Pt}$  particles. As the combustion activity was closely associated with the  $\text{Pt}$  particle size, highly dispersed  $\text{Pt}$  nanoparticles were thought to play a key role in the low-temperature light-off of  $\text{NH}_3$ . For selectivity, the proximate  $\text{CuAl}_2\text{O}_4$  in  $\text{CuO}_x/\text{Pt}/\text{Al}_2\text{O}_3$  enhanced the  $\text{NH}_3$ - $\text{NO}$  to  $\text{N}_2$  reaction, and the catalyst prevented the dissociative adsorption of  $\text{NH}_3$  to  $\text{NH}$ , which was regarded as an intermediate species obtained during the  $\text{N}_2\text{O}$  production. Therefore,  $\text{CuO}_x/\text{Pt}/\text{Al}_2\text{O}_3$  exhibits high  $\text{N}_2$  selectivity.

## Conflicts of interest

There are no conflicts to declare.

## Acknowledgements

This research was supported by JST, PRESTO (JPMJPR1344) and JSPS (18K14326). This work was partly supported by JST-Mirai





Program and the Advanced Characterization Platform of the Nanotechnology Platform Japan sponsored by the Ministry of Education, Culture, Sports, Science and Technology (MEXT), Japan. The XAFS experiments were performed at BL9A with the approval of PF, KEK (Proposal No. 2016G527), and at the BL01B1 of SPring-8 with the approval of JASRI (Proposal No. 2017A1050).

## Notes and references

- 1 P. Glarborg, A. Jensen and J. Johnsson, *Prog. Energy Combust. Sci.*, 2003, **29**, 89–113.
- 2 (a) J. Andersson and J. Lundgren, *Appl. Energy*, 2014, **130**, 484–490; (b) Y. Bicer, I. Dincer, C. Zamfirescu, G. Vezina and F. Raso, *J. Cleaner Prod.*, 2016, **135**, 1379–1395; (c) S. Giddey, S. Badwal, C. Munnings and M. Dolan, *ACS Sustainable Chem. Eng.*, 2017, **5**, 10231–10239.
- 3 (a) A. Hayakawa, T. Goto, R. Mimoto, T. Kudo and H. Kobayashi, *Mech. Eng. J.*, 2015, **2**, 14–00402; (b) R. Murai, R. Omori, R. Kano, Y. Tada, H. Higashino, N. Nakatsuka, J. Hayashi, F. Akamatsu, K. Iino and Y. Yamamoto, *Energy Procedia*, 2017, **120**, 325–332.
- 4 (a) S. Hinokuma, *et al.*, *Chem. Lett.*, 2016, **45**, 179–181; (b) S. Hinokuma, *et al.*, *J. Phys. Chem. C*, 2016, **120**, 24734–24742; (c) S. Hinokuma, *et al.*, *J. Phys. Chem. C*, 2017, **121**, 4188–4196; (d) S. Hinokuma, *et al.*, *J. Ceram. Soc. Jpn.*, 2017, **125**, 770–772; (e) S. Hinokuma, *et al.*, *Catal. Commun.*, 2018, **105**, 48–51; (f) S. Hinokuma, *et al.*, *Catal. Today*, 2018, **303**, 2–7; (g) S. Hinokuma, *et al.*, *J. Catal.*, 2018, **361**, 267–277.
- 5 (a) L. Gang, B. Anderson, J. van Grondelle, R. van Santen, W. van Gennip, J. Niemantsverdriet, P. Kooyman, A. Knoester and H. Brongersma, *J. Catal.*, 2002, **206**, 60–70; (b) M. Yang, C. Wu, C. Zhang and H. He, *Catal. Today*, 2004, **90**, 263–267; (c) J. Lee, Y. Lim, B. Park, A. Adelodun and Y. Jo, *Bull. Korean Chem. Soc.*, 2015, **36**, 162–167.
- 6 (a) R. Burch and B. Southward, *J. Catal.*, 2000, **195**, 217–226; (b) R. Burch and B. Southward, *Chem. Commun.*, 2000, 1115–1116; (c) H. Kusar, A. Ersson, M. Vosecky and S. Jaras, *Appl. Catal., B*, 2005, **58**, 25–32; (d) G. Olofsson, A. Hinz and A. Andersson, *Chem. Eng. Sci.*, 2004, **59**, 4113–4123; (e) G. Olofsson, L. Wallenberg and A. Andersson, *J. Catal.*, 2005, **230**, 1–13; (f) M. Sun, S. Wang, Y. Li, Q. Wang, H. Xu and Y. Chen, *J. Taiwan Inst. Chem. Eng.*, 2017, **78**, 401–408; (g) M. Jabłońska, *Catal. Commun.*, 2015, **70**, 66–71.
- 7 S. Lin, A. Gluhoi and B. Nieuwenhuys, *Catal. Today*, 2004, **90**, 3–14.
- 8 M. Lippits, A. Gluhoi and B. Nieuwenhuys, *Catal. Today*, 2008, **137**, 446–452.
- 9 H. Suzuki, M. Shimizu, H. Kamiya, T. Ota and M. Takahashi, *Adv. Powder Technol.*, 1997, **8**, 311–323.
- 10 B. D. Cullity, *Elements of X-RAY DIFFRACTION*, Addison-Wesley Publishing Company, Inc., Philippines, 1978.
- 11 (a) M. Hatanaka, N. Takahashi, T. Tanabe, Y. Nagai, A. Suda and H. Shinjoh, *J. Catal.*, 2009, **266**, 182–190; (b) J. Anderson, R. Daley, S. Christou and A. Efstathiou, *Appl. Catal., B*, 2006, **64**, 189–200; (c) Y. Nagai, T. Hirabayashi, K. Dohmae, N. Takagi, T. Minami, H. Shinjoh and S. Matsumoto, *J. Catal.*, 2006, **242**, 103–109.
- 12 (a) Y. Zhao and D. G. Truhlar, *Theor. Chem. Acc.*, 2008, **120**, 215–241; (b) A. Schäfer, H. Horn and R. Ahlrichs, *J. Chem. Phys.*, 1992, **97**, 2571–2577; (c) D. Andrae, U. Häussermann, M. Dolg, H. Stoll and H. Preuss, *Theor. Chim. Acta*, 1990, **77**, 123–141; (d) R. Ahlrichs, M. Bär, M. Häser, H. Horn and C. Kölmel, *Chem. Phys. Lett.*, 1989, **162**, 165–169; (e) TURBOMOLE, A development of University of Karlsruhe and Forschungszentrum Karlsruhe GmbH, 1989–2007, TURBOMOLE GmbH, since 2007, available from <http://www.turbomole.com>; (f) K. Eichkorn, F. Weigend, O. Treutler and R. Ahlrichs, *Theor. Chem. Acc.*, 1997, **97**, 119–124.
- 13 (a) F. Giordanino, E. Borfecchia, K. Lomachenko, A. Lazzarini, G. Agostini, E. Gallo, A. Soldatov, P. Beato, S. Bordiga and C. Lamberti, *J. Phys. Chem. Lett.*, 2014, **5**, 1552–1559; (b) U. Deka, A. Juhin, E. Eilertsen, H. Emerich, M. Green, S. Korhonen, B. Weckhuysen and A. Beale, *J. Phys. Chem. C*, 2012, **116**, 4809–4818.
- 14 Z. Tian, Y. Li, L. Zhang, P. Glarborg and F. Qi, *Combust. Flame*, 2009, **156**, 1413–1426.
- 15 (a) S. Yang, Y. Liao, S. Xiong, F. Qi, H. Dang, X. Xiao and J. Li, *J. Phys. Chem. C*, 2014, **118**, 21500–21508; (b) Y. Liu, T. Gu, X. Weng, Y. Wang, Z. Wu and H. Wang, *J. Phys. Chem. C*, 2012, **116**, 16582–16592; (c) L. Darvell, K. Heiskanen, J. Jones, A. Ross, P. Simell and A. Williams, *Catal. Today*, 2003, **81**, 681–692; (d) G. Busca, L. Lietti, G. Ramis and F. Berti, *Appl. Catal., B*, 1998, **18**, 1–36; (e) J. Amores, V. Escibano, G. Ramis and G. Busca, *Appl. Catal., B*, 1997, **13**, 45–58; (f) G. Ramis, L. Yi, G. Busca, M. Turco, E. Kotur and R. Willey, *J. Catal.*, 1995, **157**, 523–535; (g) B. Duffy, H. Curryhyde, N. Cant and P. Nelson, *J. Catal.*, 1994, **149**, 11–22.
- 16 (a) V. Dasireddy, B. Likozar and J. Valand, *Appl. Catal., B*, 2018, **237**, 1044–1058; (b) S. Lambert, C. Cellier, P. Grange, J. Pirard and B. Heinrichs, *J. Catal.*, 2004, **221**, 335–346.
- 17 G. Busca, *Catal. Today*, 2014, **226**, 2–13.
- 18 K. Okada, A. Hattori, T. Taniguchi, A. Nukui and R. Das, *J. Am. Ceram. Soc.*, 2000, **83**, 928–932.
- 19 M. Ferrandon, B. Ferrand, E. Bjornbom, F. Klingstedt, A. Neyestanaki, H. Karhu and I. Vayrynen, *J. Catal.*, 2001, **202**, 354–366.

